



Contactless Manipulation and Raman Analysis of Cometary Analogs and Micrometeorites by Acoustic Levitation

S. Ferretti^{1,2,7}, S. Marrara^{3,4}, D. Bronte Ciriza^{3,4}, A. Magazzù⁴, A. Foti⁴ , P. G. Gucciardi⁴, A. Musolino^{2,8} , L. Folco⁵ , V. Della Corte⁶, A. Rotundi^{1,2}, R. Saija^{3,4}, A. Mandanici^{3,4} , O. M. Maragò⁴ , and M. G. Donato⁴

¹ Dipartimento di Scienze e Tecnologie, Università degli Studi di Napoli "Parthenope," Naples, Italy

² Istituto di Astrofisica e Planetologia Spaziali, Istituto Nazionale di Astrofisica, Rome, Italy

³ Dipartimento di Scienze Matematiche e Informatiche, Scienze Fisiche e Scienze della Terra, Università degli Studi di Messina, Messina, Italy; andrea.mandanici@unime.it

⁴ CNR-IPCF, Istituto per i Processi Chimico-Fisici, Messina, Italy; maria.donato@cnr.it, onofrio.marago@cnr.it

⁵ Dipartimento di Scienze della Terra, Università di Pisa, Pisa, Italy

⁶ Oss. Astronomico Capodimonte, Istituto Nazionale di Astrofisica, Napoli, Italy

Received 2024 June 8; revised 2024 August 9; accepted 2024 August 20; published 2024 October 17

Abstract

Extraterrestrial material collected during space missions is highly exposed to contamination issues during on-Earth analysis. Although high-protection-level protocols were developed, to minimize the contamination due to sample manipulation and the substrate contribution an optimal strategy is to perform in situ analysis with contactless techniques. Optical and acoustic trapping represent ideal candidates for contactless manipulation and analysis of nanometer-to-millimeter-sized particles. Here, we show results of the manipulation of cometary analogs and micrometeorite samples using a single-axis acoustic levitator. The investigation of the particle dynamics in the trap allows the calculation of the trap spring constants that are found in the mN/m range. In addition, we collect the Raman spectra of two levitated fragments of Saratov meteorite, demonstrating that acoustic levitation can be effectively used for the contactless and low-contamination characterization of samples of interest in astrophysics.

Unified Astronomy Thesaurus concepts: [Interstellar dust \(836\)](#)

1. Introduction

In the mid-20th century, the study of cosmic dust (interplanetary and interstellar) turned out to be fundamental for the understanding of our solar system and the evolution of stars (C. Cecchi-Pestellini et al. 2012; B. A. McGuire 2018), as well as the origin of life (G. J. Flynn et al. 2003). In order to maximize the information extracted from such samples, high analytical resolution and minimum contamination are essential. However, manipulation and characterization of extraterrestrial dust particles are still a challenge (S. A. Sandford 2011; Q. H. S. Chan et al. 2020; J. L. Eigenbrode et al. 2021; T. Yada et al. 2023).

Many tons of extraterrestrial material fall on Earth every year. The majority of this material consists of micrometeorites, typically less than 2 mm in size, which are recovered at Earth's surface (M. J. Genge et al. 2008; L. Folco & C. Cordier 2015; S. Taylor et al. 2016; M. van Ginneken et al. 2024). Another significant contribution is given by the interplanetary dust particles (IDPs), mainly collected in the upper stratosphere (F. J. M. Rietmeijer 2002; V. Della Corte et al. 2012, 2014), ranging from hundreds of nanometers (V. D. Corte et al. 2013; F. J. M. Rietmeijer et al. 2016) up to hundreds of microns (S. Messenger et al. 2015).

Sample-return space missions are designed to gather contamination-free IDPs for successive on-Earth analysis

(D. E. Brownlee et al. 2003; Y. Tsuda et al. 2013; M. Yoshikawa et al. 2021), which can be performed more easily and with state-of-the-art analytical techniques (C. L. Smith et al. 2021). To protect the collected samples from terrestrial contamination, highly inert handling protocols and strategies are needed. Consolidated techniques like optical tweezers (OTs; A. Ashkin 2006; P. H. Jones et al. 2015) or magnetic levitation (A. K. Geim et al. 1999; A. El Hajjaji & M. Ouladsine 2001) allow the contactless manipulation of small particles, even though they might have strict requirements for the nature of the sample or the experimental conditions (Z. Gong et al. 2018a, 2018b).

Another versatile technique for contactless manipulation is acoustic levitation (AL), which exploits forces arising from the momentum carried by sound waves to trap and manipulate micron-to-millimeter-sized particles of different composition (H. Bruus 2012; J. F. P. Ospina et al. 2022) in air (D. Koyama & K. Nakamura 2010; D. Foresti & D. Poulidakos 2014; G. Memoli et al. 2017) or in a fluid (X. Ding et al. 2012; D. Baresch et al. 2016; D. Baresch & V. Garbin 2020). Compared to their optical counterpart, AL can levitate larger particles. Moreover, the higher trapping forces per unit input power strongly reduce the heating issues that sometimes affect OT when trapping light-absorbing particles (H. Rubinsztein-Dunlop et al. 1998). All these features earned AL interesting applications in biomedical research (K. Dholakia et al. 2020a, 2020b), life sciences (G. Thalhammer et al. 2016; A. Ozcelik et al. 2018), physics of liquids (D. Zang et al. 2017), and soft matter (L. Meng et al. 2019; Z. Ma et al. 2020). Coupling with Raman spectroscopy has allowed the study of gold and silver nanoparticle synthesis (J. Park et al. 2023), the droplet manipulation on superhydrophobic surfaces (T. Luo et al. 2023), the enrichment of trace analytes in levitated droplets (X. Chen et al. 2022), the crystallization process, not available in the bulk phase, of a supersaturated droplet in air (T. Yamaguchi et al. 2023), the secondary structure changes of

⁷ Present address: Institute for Complex Systems (ISC-CNR), National Research Council, c/o Department of Physics, Sapienza University of Rome, 00185 Rome, Italy.

⁸ Present address: Aix Marseille Université, CNRS, IRD, INRAE, CEREGE, Aix-en-Provence, France.

biological molecules in drying droplets (J. F. A. Perlitz et al. 2022), the in situ chemical reaction monitoring in a chamber under controlled pressure and radiation conditions (B. B. Dangi & D. J. Dickerson 2021), and the diagnostic and monitoring of red blood cells (L. Puskar et al. 2007).

Acoustic levitators are most commonly arranged in single-axis configuration (R. R. Whymark 1975), with an acoustic emitter (Langevin horn; S. Lin 1995) and a reflector (resonant cavity) or two opposite emitters (nonresonant cavity). In both cases, the acoustic standing waves forming in the cavity between the two elements can trap small particles in the nodes. Langevin horns, however, are difficult to tune to a specific resonant frequency. In addition, the high voltages required by the device cause it to heat up, making the system sensitive to temperature (R. H. Morris et al. 2019).

More recent acoustic levitators are based on arrays of ultrasonic emitters (USEs), which are arranged in different geometries to implement either single-axis or multi-axis manipulators (A. Marzo et al. 2015). In particular, the type of emitter sets the frequency of the acoustic wave, while its amplitude (within a specific range) and phase can be regulated. Specific phase patterns applied to the USE arrays allow to precisely handle the location of one or more traps for real-time simultaneous manipulation of multiple particles in 3D (A. Marzo & B. W. Drinkwater 2019). A single-axis acoustic levitator based on the concept just mentioned is the TinyLev (A. Marzo et al. 2017). It is made of 72 low-voltage (20 V max.) commercially available USEs operating at 40 kHz in air and arranged in two opposite spherical-cap arrays. In the space between the arrays, an acoustic standing wave results from the superposition of the counterpropagating acoustic beams. The nodes, vertically aligned along the symmetry axis of this device, represent multiple traps that can be collectively displaced by regulating the phase delay between the two USE arrays. The system is virtually unaffected by changes in temperature and humidity and can be operated easily and for extended periods of time. Arrays of ultrasonic transducers have been already used to levitate and control the orientation of asymmetric particles (P. Helander et al. 2020) and the synthesis of highly sensitive Raman sensors (Y. Liu et al. 2023; Z. Ding et al. 2024).

The TinyLev device can trap objects at a density as high as 3.9 g cm^{-3} with an input power of approximately 20 W (A. Marzo et al. 2017). The capability of this setup to contactless trap in air millimeter particles having a density similar to that of many micrometeorites and materials found in comet and asteroid samples returned to Earth, as well as IDPs, is particularly interesting in low-contamination studies of extraterrestrial particles suggesting that comparative measurements obtained on terrestrial analogs could be indicative of unknown extraterrestrial particle properties, such as density or mineralogical content.

In this work, we use a TinyLev setup to trap and manipulate mm-sized hydrated (kaolinite) and anhydrous (augite and jadeite) silicates and a sample from the Transantarctic Mountains (TAM) micrometeorite collection (P. Rochette et al. 2008). They have been chosen as analogs of cometary dust and asteroid-like materials (L. Colangeli et al. 1995; A. Rotundi et al. 2002; M. Ferrari et al. 2014), to test AL capability for the contactless manipulation and characterization of dust coming from sample-return missions. The dynamics of the trapped particles is tracked and analyzed by using the

power spectral density (PSD) of the signals obtained (S. Marrara et al. 2023). Finally, we couple the TinyLev to a portable Raman spectrometer to collect the spectroscopic signal of levitated fragments of the L4 ordinary chondrite Saratov meteorite (M. M. Grady 2000), characterizing their mineralogical content.

2. Materials and Methods

2.1. Experimental Strategy

The experimental setup is sketched in Figure 1(a). The TinyLev (Figure 1(b)) is at the intersection of two perpendicular optical paths. In the first path, an incoherent light source illuminates the trapped particle, whose shadow is focused with a two-lens telescope on the image plane of a CCD (Thorlabs Zelux CS165 MU/M or Basler a2a 1920-160umBAS). The frames are recorded on the PC for successive analysis. In the second path, a low-power laser beam illuminates the levitated particle and the resulting shadow is delivered, through a mirror and a telescope, on a four-quadrant photodiode (QPD; Thorlabs PDQ80A), which records particle position fluctuations in the trap (S. Marrara et al. 2023). The voltage signal acquired by the QPD is analyzed by custom-made LabView codes. Particle fluctuations in x and y directions are collected by CCD and QPD, respectively, and due to the symmetry of the trap, they are expected to be equal. Fluctuations in the axial direction z are collected on both detectors. Test measurements and calibration using styrofoam spherical particles are discussed in Appendix A.

We trapped terrestrial single minerals of size range 0.5–1 mm of (i) anhydrous silicates, augite and jadeite (Ca and Na pyroxenes) and (ii) the hydrated silicate kaolinite (phyllosilicate). An extraterrestrial sample, a micrometeorite from the TAM collection of 0.8 mm in size, has also been trapped (see Figures 2(a)–(f)). The selection of the analogs is not primarily linked to their occurrence in laboratory analysis performed on IDPs of cometary origin (A. Rotundi et al. 2007; R. Brunetto et al. 2011) or on cometary particles (A. Rotundi et al. 2014), but it has been made according to their different densities (e.g., augite and kaolinite) or to test materials representative of possible processing, such as jadeite, which is interesting as its presence in comets can contribute to disentangle evolution paths followed by comet formation models, providing clues on solar system formation models (M. Fulle et al. 2016; J. Blum et al. 2017).

As shown in Figure 2, the contrast of the video frames is sufficiently high to be exploited for the analysis of the particle dynamics. We wrote custom video-tracking scripts to extract the particle position, orientation, and dimensions. First of all, in order to verify that the particle is in the field of view (FOV), we check frame by frame that there are regions with high contrast (i.e., the difference between maximum and minimum intensity values assigned to each pixel is higher than a reference value). Then, a threshold is applied to the frame to make it binary, and a geometrical analysis follows. We describe as an example the operations on the augite #2 particle frame reported in Figure 2(b).

We verify that the frame contrast is higher than a custom reference value to check that the particle did not escape the FOV. Then, we apply a custom threshold to the frame to convert it into a binary map $\rho(x, z)$, which is 1 where there is the object and 0 all around (Figure 2(g)). The normalized

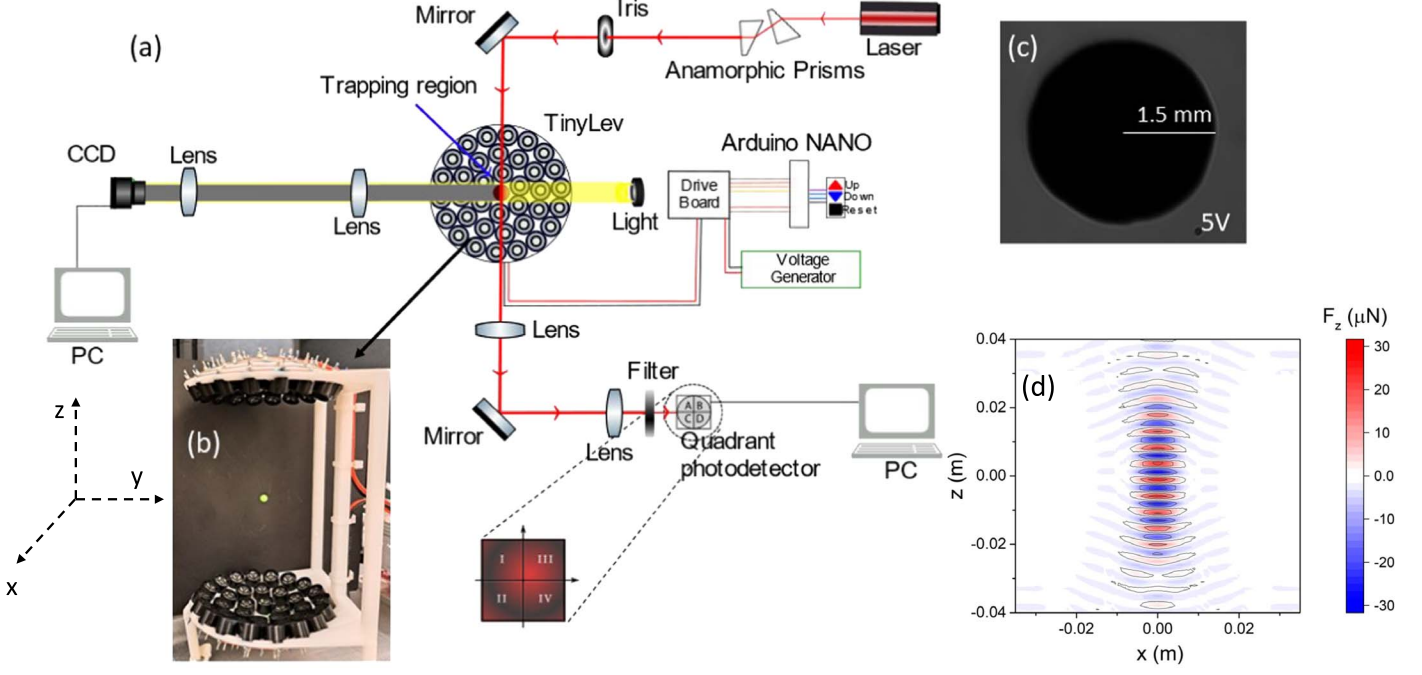


Figure 1. Experimental setup. In (a), the TinyLev acoustic levitator (shown in (b), along with the trap reference system) is set at the intersection of two optical paths that are perpendicular to each other. The levitated particle (as an example, in (c) a millimeter-sized styrofoam particle is shown) is illuminated by a lamp (yellow optical path), and its shadow is collected by a CCD camera. Alternatively, the particle is illuminated by a laser (red optical path), and its shadow is collected by a QPD, which records the particle position fluctuations in the trap. Digital processing of the recorded shadow (for CCD-based measurements) or homemade LabView codes (for QPD-based measurements) allow to reconstruct the particle dynamics in the trap. In (d), a map of the axial acoustic force on a styrofoam bead at $R = 1$ mm, based on the Gor'kov potential, is shown.

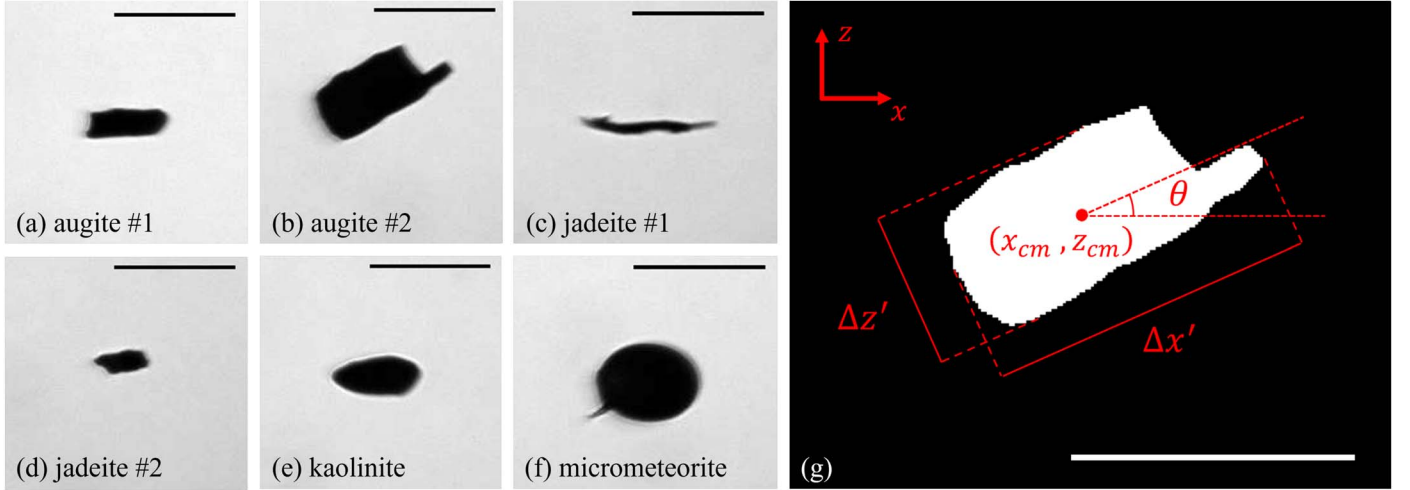


Figure 2. Samples. (a)–(f) Frames from the tracking videos showing the shadow of the samples manipulated with the TinyLev acoustic levitator: two augite particles (a, b), two jadeite particles (c, d), a kaolinite particle (e), and a micrometeorite sample (f). A scheme of the geometric features extracted from analysis is also reported (g): the object center of mass (x_{cm}, z_{cm}) , its orientation θ , and its dimensions $(\Delta x', \Delta z')$ (in the reference frame oriented as the object). Scale bars are 1 mm long.

binary map $\frac{\rho(x, z)}{\iint \rho(x, z) dx dz}$ can be handled as a probability density function whose moments can be meaningful for the analysis. The first moment relative to the x coordinate, for example, is defined as

$$\mu_x^1 = \frac{\iint \rho(x, z) x dx dz}{\iint \rho(x, z) dx dz} = \langle x \rangle = x_{cm} \quad (1)$$

and represents the average value of the x coordinate. In the same way, we can compute the $\langle z \rangle$ value in order to retrieve the 2D center of mass (x_{cm}, z_{cm}) of the object.

The 2nd moment of the probability density function leads to the covariance matrix:

$$C_{ij} = \frac{\iint \rho(x, z) (x_i - \langle x_i \rangle) (x_j - \langle x_j \rangle) dx dz}{\iint \rho(x, z) dx dz}, \quad (2)$$

where $x_{i,j}$ can be either x or z . The eigenvectors resulting from the covariance matrix diagonalization encode the object orientation. In particular, we consider the eigenvector corresponding to the greater eigenvalue as our reference to retrieve the angle θ of the particle. In Figure 2(g), for instance, $\theta = 24.3$ deg. We apply a rotation of θ to the coordinate system (x, z) to obtain a new coordinate system (x', z') oriented as the object (x' parallel to the major axis of the object). In the new reference, the object dimensions $(\Delta x', \Delta z')$ are computed as the difference between the maximum and minimum coordinates for which $\rho(x', z') = 1$. In the case of panel (g), $\Delta x' = 1.16$ mm and $\Delta z' = 0.56$ mm.

Several measurements were performed for each of the available materials, each time powering the TinyLev device with different voltages to study the particle dynamics at different trapping stiffness. The voltage values were selected according to the particle stability in the trap, a condition that changes from particle to particle as it strongly depends on the coupling between the acoustic field and the particle shape and material.

Particle dynamics have been studied with both a CCD camera and a QPD. From the position tracks $x_i(t)$, with $x_i = x, y, z$, the PSD of each axis can be retrieved as

$$\text{PSD}_{x_i}(f) = \frac{1}{T} \left| \int_0^T e^{-i2\pi ft} x_i(t) dt \right|^2, \quad (3)$$

where T is the time interval of data recording and f is the oscillation frequency. Due to random perturbations, the particle oscillates around its equilibrium position. To a first approximation, its dynamics can be modeled as those of a simple harmonic oscillator. Given the particle mass m and its oscillation frequency f_i (with $i = x, y, z$), the force constant k_i of the acoustic trap can be retrieved as

$$k_i = (2\pi f_i)^2 \cdot m. \quad (4)$$

2.2. Calculation of the Acoustic Force

2.2.1. Modeling the Ultrasonic Emission

To realize the acoustic trap, each j -th transducer is modeled as a circular piston, whose far-field acoustic pressure p_j at a target point $A(x, y, z)$ is given by

$$p_j = e^{i\phi_j} M_j, \quad (5)$$

with ϕ_j representing the initial phase of each transducer and

$$M_j = P_0 V_{pp} \frac{2J_1(\kappa a \sin \theta_j)}{\kappa a \sin \theta_j} \frac{1}{d_j} e^{i\kappa d_j}. \quad (6)$$

Here, d_j is the generic distance of the j -th transducer from the A point, $\kappa = \frac{2\pi f}{c_0}$ is the wavevector, f is the frequency of the signal emitted by the transducer ($f = 40$ kHz), $c_0 = 346$ m s⁻¹ is the velocity of sound in air, a is the transducer radius, θ_j is the angle between d_j and the z -axis, J_1 is the Bessel function of the first kind, $P_0 = 0.17$ Pa m V⁻¹ is a power constant typical of the transducer, and V_{pp} is the voltage sent by the power supply. The transducers belonging to the same dome emit in phase, i.e., they have the same ϕ_j , but the signal arriving at the A point has a phase controlled by the transducer position on the dome (that is, on the θ_j angle). The pressure field produced by a dome is obtained as $p = \sum_j p_j$; this can interfere with the signal

coming from the other dome giving a nearly standing wave pattern of the total pressure field in the axial direction. A shift in the initial phase ϕ_j between the two domes allows to move the position of the nodes of the standing wave along z .

2.2.2. Gor'kov Potential

In the limit of spherical particles with size lower than the wavelength λ of the acoustic wave, it is possible to define a potential energy function U , known as the Gor'kov potential, as

$$U = K_1(|p|^2) - K_2(|p_x|^2 + |p_y|^2 + |p_z|^2), \quad (7)$$

with

$$K_1 = \frac{1}{4} V \left(\frac{1}{\rho_0 c_0^2} - \frac{1}{\rho_p c_p^2} \right) \quad (8)$$

and

$$K_2 = \frac{3}{4} V \frac{\rho_p - \rho_0}{\rho_0 \omega^2 (\rho_0 + 2\rho_p)}, \quad (9)$$

where $V = 4\pi R^3/3$ is the volume of the spherical particle, $\omega = 2\pi c_0/\lambda$ is the angular frequency of the acoustic pressure wave, $\lambda = c_0/f = 8.6$ mm, ρ_0 and ρ_p are the density of the fluid and the density of the particle, respectively, c_0 and c_p are the velocity of ultrasonic waves in the fluid and in the particle, respectively, p is the complex acoustic pressure field, and p_x , p_y , and p_z are the partial derivatives of the pressure with respect to the coordinates x , y , and z , respectively.

Assuming that the acoustic radiation force arises from Gor'kov potential, we have

$$\vec{F}_{\text{rad}} = -\nabla U, \quad (10)$$

from which

$$F_i = -\frac{\partial U}{\partial x_i}, \quad (11)$$

with $(x_i = x, y, z)$ and also

$$k_i = -\frac{\partial}{\partial x_i} \left(-\frac{\partial U}{\partial x_i} \right) = \frac{\partial^2 U}{\partial x_i^2}. \quad (12)$$

In the following, the Gor'kov potential approximation has been used to estimate the trap spring constants on an augite sphere with volume equal to the augite #1 sample (Figure 2 (a)) by considering $\rho_p = \rho_{\text{aug}} = 3.4$ g cm⁻³ as the average augite density (D. Barthelmy 1997; J. Ralph 2000) and $c_p = c_{\text{aug}} = 3740$ m s⁻¹ as its average sound velocity (O. L. Anderson & R. C. Liebermann 1966).

3. Results and Discussion

We focus our analysis on an augite fragment as an example of a terrestrial cometary analog and on a micrometeorite as an example of an extraterrestrial dust sample. The study on other analogs is shown in Appendix B.

3.1. Augite Fragment

Augite is a Ca-rich pyroxene that can be found in primitive meteorites (A. J. Brearley & R. H. Jones 1998), comets (D. Joswiak et al. 2017), and IDPs (F. J. Rietmeijer 1998). An augite particle (augite #1 sample, Figure 2(a)) was trapped at

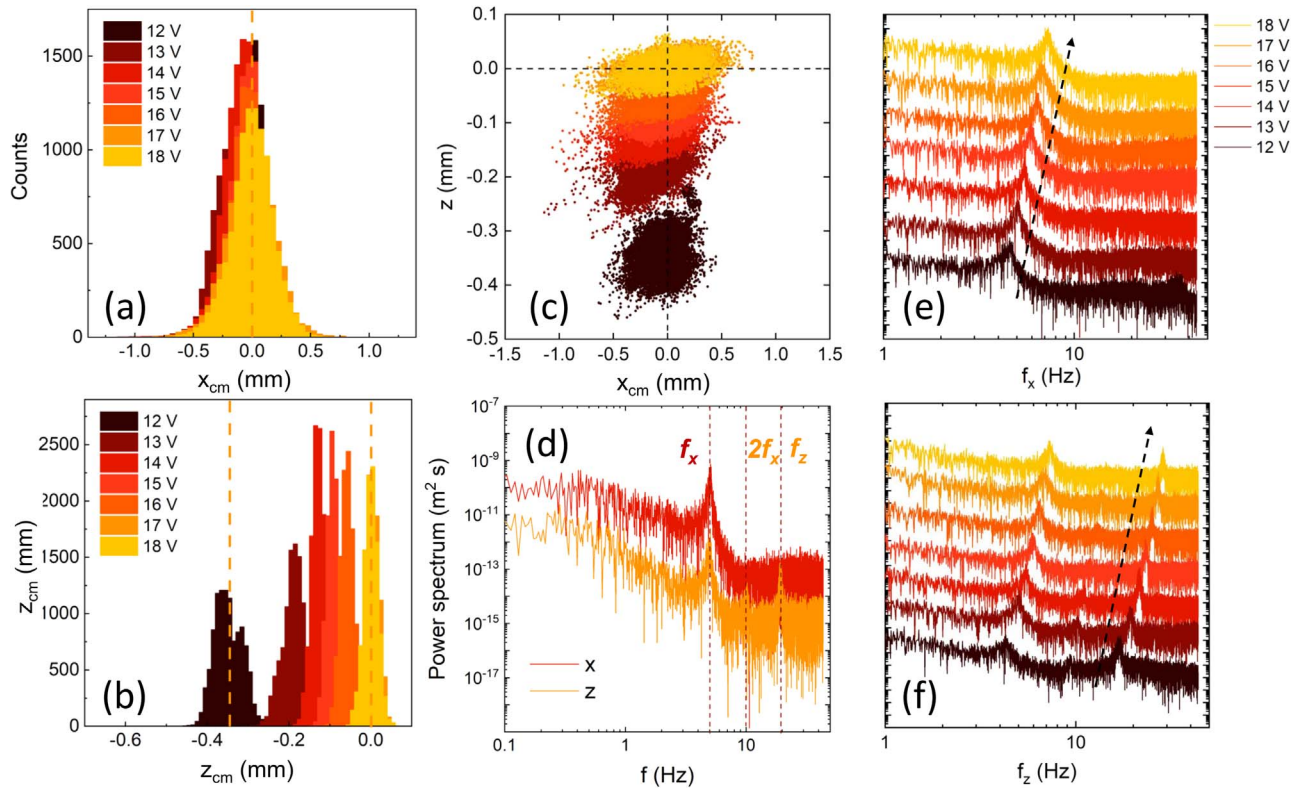


Figure 3. Augite #1. Histograms of the center-of-mass positions along the x - (a) and z - (b) axes. While the transverse confinement is nearly independent of the supplied voltage, the axial confinement increases at increasing V_{pp} . The coordinates of the reference origin are the average (x_{cm} , z_{cm}) positions of the particle at the maximum trapping voltage. In (c), the (x_{cm} , z_{cm}) coordinates of the center of mass are shown. In (d) the PSDs of x_{cm} and z_{cm} fluctuations are shown at 13 V excitation voltage. In the PSD along the x direction (red line), a single peak at $f_x = 5.1$ Hz is observed. In the PSD along the z direction (orange line), three peaks at approximately 5.1, 10.2, and 19.4 Hz are observed. Moreover, the overall signal is 2 orders of magnitude lower than in the PSD along the x direction. In (e) and (f) the PSDs of the augite #1 center of mass fluctuations along x and z are shown, respectively, at all excitation voltages used. The arrows are guides for the eye highlighting the increase of PSD peak frequencies at increasing voltages. Data are vertically displaced for clarity.

V_{pp} ranging from 12 to 18 V. Figure 3 shows the histograms of the positions occupied along the x - and z -axes (panels (a) and (b), respectively) and the (x , z) coordinates of the center of mass for all trapping voltages (panel (c)). The distribution of the acoustic field generated by the TinyLev results in a stronger confinement of the particle in the axial direction (i.e., vertically) rather than on the horizontal plane. This fact reflects in a wider distribution of the particle positions cloud along x rather than along z (see the greater width of histograms in panels (a) than in panel (b)). Moreover, while in the x direction the particle fluctuates around the origin of the reference for all voltages, the mean position along z drops more and more as the voltage decreases (panel (c)). A lower voltage corresponds to a lower acoustic force; therefore, the effect of gravity becomes more relevant and the particle falls down in a new equilibrium position. In addition, since in a weaker trap the particle is less confined along the vertical axis, its fluctuations around its own mean position become more isotropic.

In Figure 3(d) the power spectra of the CCD tracking signals along x and z directions obtained on augite #1 particle at 13 V power supply are shown. The peak at approximately $f_x = 5.1$ Hz is observed in both PSDs. As already pointed out (S. Marrara et al. 2023), the occurrence of the same peak on both the spectra is due to the anisotropic scattering of the acoustic radiation forces due to the strongly anisotropic particle shape, causing a cross talk between x and z particle fluctuations. The peak at the highest frequency in the PSD along the z direction is approximately centered at $f_z = 19$ Hz. It

is associated to the center of mass fluctuations along the axial direction, where the acoustic confinement is stronger. Moreover, in the PSD $_z$ spectrum, a small peak at approximately $2 \times f_x$ is also observed. Similar peaks are not observed in the PSDs of spherical particles. It is worth noting that the dynamics of the nonspherical particle are characterized by both the center of mass fluctuations and particle rotations. Unlike in optical trapping experiments (P. H. Jones et al. 2009), in our case the timescales of particle translations and rotations are similar, and their contributions to the PSD spectrum are not easily distinguishable. We can tentatively associate the peaks at $f_x = 5.1$ Hz and $2 \times f_x = 10.2$ Hz to the coupling of translations and rotations of the center of mass of the particle and, in particular, the lower frequency to the mixed translational-rotational movements of the asymmetric part of the particle and the higher one to its symmetric part (P. H. Jones et al. 2009). It is worth noting that the peak at $2 \times f_x$ is not observed in the PSD spectrum along the x direction because this peak is characterized by a 2 orders of magnitude lower signal value than PSD $_x$ in the correspondent frequency range.

In Figures 3(e) and (f) the PSD spectra registered on augite #1 sample are shown at all the voltages supplied. The increase of the f_i at increasing V_{pp} is observed. From the measured values of f_x (or f_y , due to the cylindrical symmetry of the trap) and f_z it is possible to estimate the transversal and axial trap spring constants, if the particle mass is known. To calculate it, we measure particle dimensions with our tracking software and use the augite density value reported in the literature

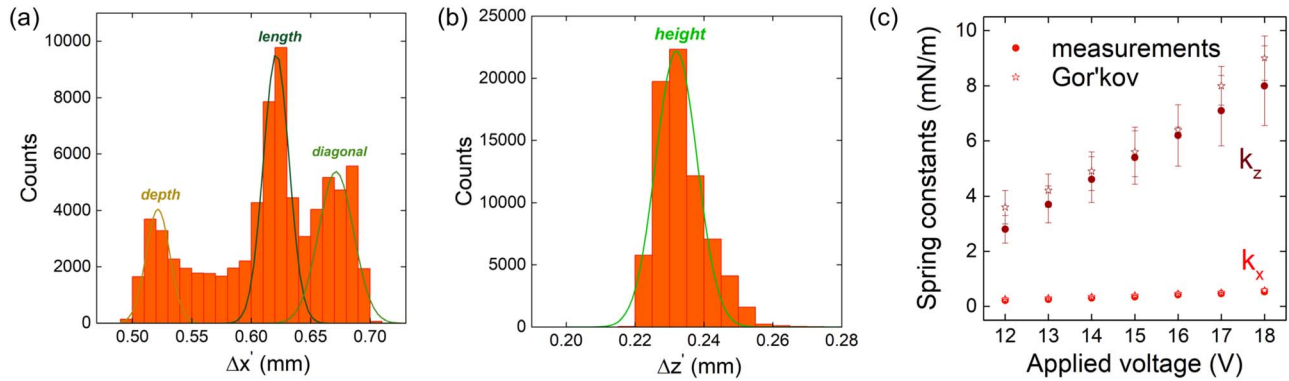


Figure 4. Augite #1. Dimensions of the particle along the axes x' (a) and z' (b) of the reference system integral with the particle. For this plot we integrated the data resulting from all the attempts at different voltages. (c) Trap spring constants on augite #1 sample (dots) and corresponding calculated values (stars) using the Gor'kov potential. A remarkable agreement is found.

(D. Barthelmy 1997; J. Ralph 2000). The particle dimensions were extracted from the data resulting from all the measurements at different voltages. The analysis returned the data reported in Figures 4(a) and (b). The histogram in the left panel shows the particle dimensions along the x' -axis, and since the object rotates also around the z -axis, both horizontal dimensions (depth $\Delta x'_d$ and length $\Delta x'_L$) should be included. However, three peaks are shown, of which the left one represents the lower horizontal dimension ($\Delta x'_d = 0.52\text{mm}$). Regarding the other peaks, we consider the one in the middle to represent the longer horizontal dimension ($\Delta x'_L = 0.62\text{mm}$). The right peak could come from those frames in which the particle rotates and the length of the cross section is the diagonal of the parallelepiped-like object. Finally, the particle dimension along the z' -axis has a single peak at $\Delta z' = 0.23\text{mm}$. Approximating the particle to a parallelepiped, its volume can be calculated as $V = 0.075 \cdot 10^{-3} \pm 5 \cdot 10^{-7}\text{cm}^3$, and using $\rho_{\text{aug}} = 3.4\text{g cm}^{-3}$ as the average augite density (D. Barthelmy 1997; J. Ralph 2000), the particle mass is calculated as $m = 0.255 \pm 0.002\text{mg}$. Thus, transversal and axial spring constants can be calculated by Equation (4), resulting in the data shown in Figure 4(c) as a function of the applied voltages. As already observed for spherical particles (S. Marrara et al. 2023), the trap spring constants show a linear dependence on the applied voltage, even if a quadratic dependence is expected on the basis of Equation (7). This is due to the fact that, at high voltages (approximately $>15\text{V}$), the transducers enter in a “saturation” regime, with lower signal than the one theoretically expected (A. Marzo et al. 2017). In addition, k_z is larger than k_x , due to the standing wave character along z of the pressure field. It is interesting to note that the calculation based on the Gor'kov potential (outlined in Section 2.2.2) of the trap spring constants on an augite equivalent sphere having the same volume of augite #1 sample gives very similar values to those experimentally found (stars in Figure 4(c)), thus further confirming the capability of the Gor'kov model in providing consistent results even for more massive particles than simple styrofoam beads (S. Marrara et al. 2023).

3.2. Micrometeorite

The micrometeorite (see Figure 2(f)) used in this work is a cosmic spherule recovered from the TAM. It belongs to the silicate type and barred olivine subtype (L. Folco & C. Cordier 2015). It is dominated by fine skeletal bars up to few tens of microns in thickness of forsterite (Mg-olivine), set in a glassy

silicate mesostasis bearing micron-sized magnetite crystals. The particle has been trapped at voltages between 15 and 18 V. Both the transversal and axial confinements are nearly constant at increasing V_{pp} (Figure 5(a) and (b)), due to the fact that we are trapping at relatively high voltages. At variance with the previous augite microparticle, it was not possible to trap using a voltage lower than 15 V.

The PSDs of the tracking signals along transversal and axial directions are shown in Figures 5(d) and (e). They are similar to those previously observed in the augite #1 case, with a single peak in PSD $_x$ and three peaks, corresponding to f_x , $2f_x$, and f_z in the PSD $_z$. It is interesting to note that in this case the frequency of the oscillations is slightly lower than in the augite #1 case at the corresponding voltages supplied.

In Figures 5(f) and (g) the transversal and axial size of the particle is obtained by fitting with a Gaussian the histogram of the $\Delta x'$ and $\Delta z'$ distribution. The particle has a spheroidal shape with two similar larger semiaxes, $a = 0.42 \cdot 10^{-3}\text{mm}$ and $b = 0.41 \cdot 10^{-3}\text{mm}$, in the transversal direction and a shorter semiaxis, $c = 0.3 \cdot 10^{-3}\text{mm}$, in the axial direction. Thus, the particle volume V_{met} can be easily calculated as $V_{\text{met}} = \frac{4}{3}\pi abc = 0.217 \cdot 10^{-3} \pm 6 \cdot 10^{-6}\text{cm}^3$. Based on the density ($2.9\text{--}3.7\text{gr cm}^{-3}$) of barred olivine cosmic spherules (T. Kohout et al. 2014) and in consideration that our micrometeorite should have a density larger than augite (see Appendix B), we can estimate a k_x trap spring constant comprised between $0.5 \pm 0.01\text{mN m}^{-1}$ and $0.8 \pm 0.02\text{mN m}^{-1}$ and a k_z trap spring constant comprised between $8 \pm 0.2\text{mN m}^{-1}$ and $13 \pm 0.3\text{mN m}^{-1}$ by assuming a micrometeorite density of 3.7gr cm^{-3} . Further considerations on the use of acoustical levitation for the measurement of the density of an unknown material of which only very small amounts are available (as our micrometeorite) are in Appendix B.

3.3. Acoustic Raman Levitator

A portable system consisting of an excitation laser (785 nm, up to 450 mW in power) and a Raman spectrometer (Wasatch Photonics) has been coupled to our acoustic levitator. This system uses a probe to send the excitation laser on the levitated sample and to collect the backscattered Raman signal, which is delivered to the spectrometer by means of an optical fiber (105 μm core diameter). The probe stays at a distance of approximately 1 cm from the levitated sample, not to disturb the acoustic pressure field. Individual fragments of the Saratov meteorite have been levitated in our AL. In Figure 6(a)(black

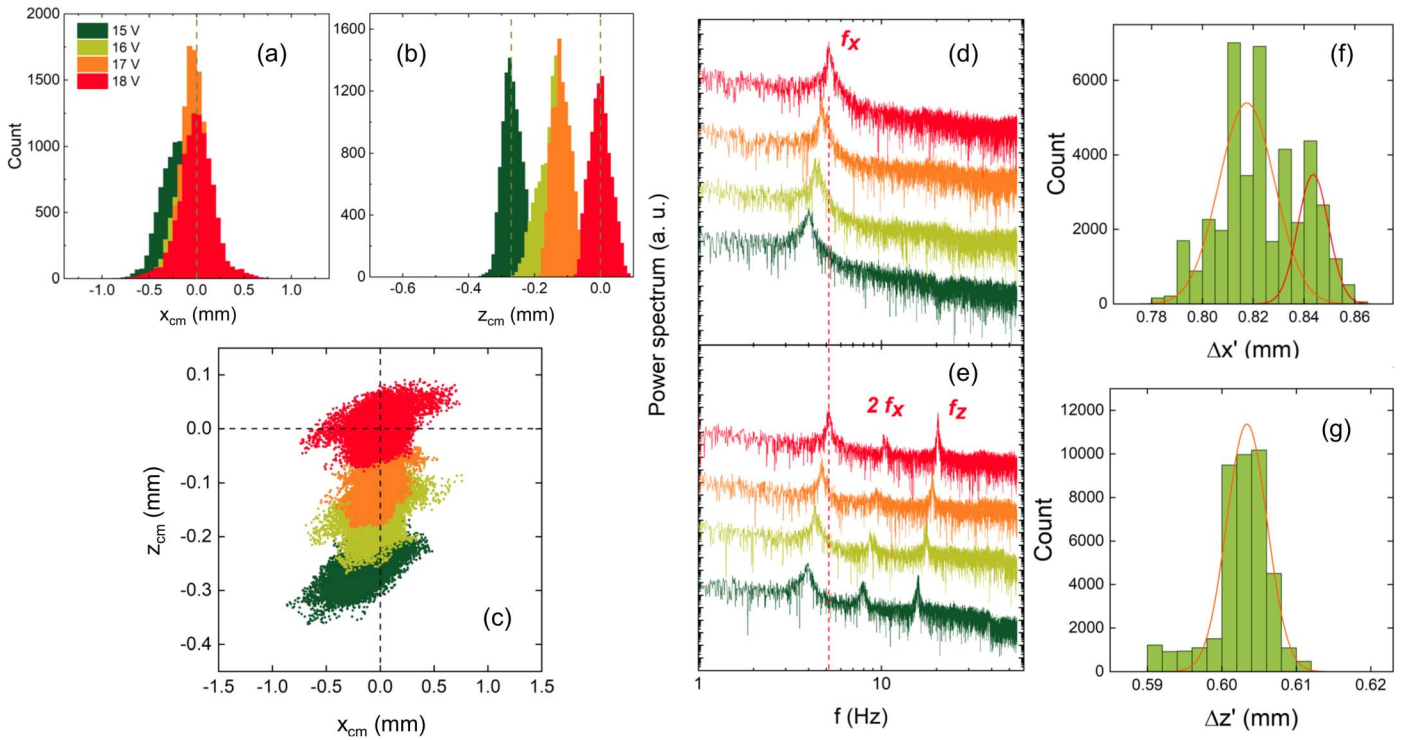


Figure 5. Micrometeorite. Histograms of the x_{cm} (a) and z_{cm} (b) coordinates of the particle center of mass for the different trapping voltages. In (b), the different axial equilibrium position at increasing V_{pp} is highlighted. In (c), the distribution of the center of mass positions is shown at all the voltages supplied. (d, e) Power spectra of the particle tracking signals along x (d) and z (e) coordinates. The peak frequencies are also indicated. Data have been displaced vertically for clarity. (f, g) Histograms of the particle size along transversal (f) and axial (g) directions. The fit curves from which the minimum and maximum transversal size (f) and axial size (g) are also shown.

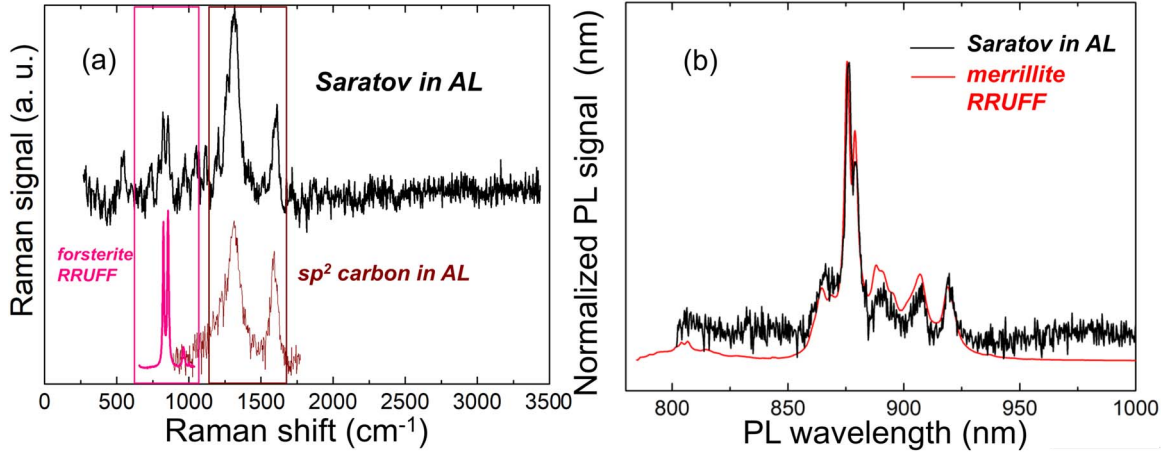


Figure 6. Spectra of levitated Saratov fragments. (a, black line) Spectrum registered on a Saratov fragment after background removal. The doublet at 819 and 855 cm^{-1} are due to the presence of forsterite (magenta curve; RRUFF R040018-3 file), while the two broader peaks at approximately 1320 and 1590 cm^{-1} are due to the presence of amorphous sp^2 -carbon phases (brown curve; spectrum obtained from a small rod of a pencil graphite levitated in our AL). (b, black line) Photoluminescence spectrum registered on a Saratov levitated fragment in AL after background removal. The signal is attributed to merrillite (red curve; RRUFF R150063 file), an anhydrous Ca-phosphate mineral that can be found in very low amounts in ordinary chondrites like Saratov.

line), a Raman spectrum obtained from one levitated fragment is shown, after removing a broad and featureless background. The subtracted spectrum is characterized by a doublet at 819 and 855 cm^{-1} , which highlights the presence of forsterite mineral (magenta line; B. Lafuente et al. 2015; RRUFFTM Project R040018-3 file) and two peaks at 1320 and 1590 cm^{-1} , which can be associated to amorphous sp^2 -hybridized carbon phases (A. C. Ferrari & J. Robertson 2001; brown line,

obtained from a levitated pencil's graphite small rod). In another fragment (Figure 6(b), black line), the presence of a huge signal (2 orders of magnitude higher than the ordinary Raman signal) has also been detected. This spectral feature is associated to the presence of the mineral merrillite (B. Lafuente et al. 2015; RRUFFTM Project R150063 file), which can be found in a very low (less than 1% volume) amount in ordinary chondrites such as Saratov. The signal is higher than the Raman

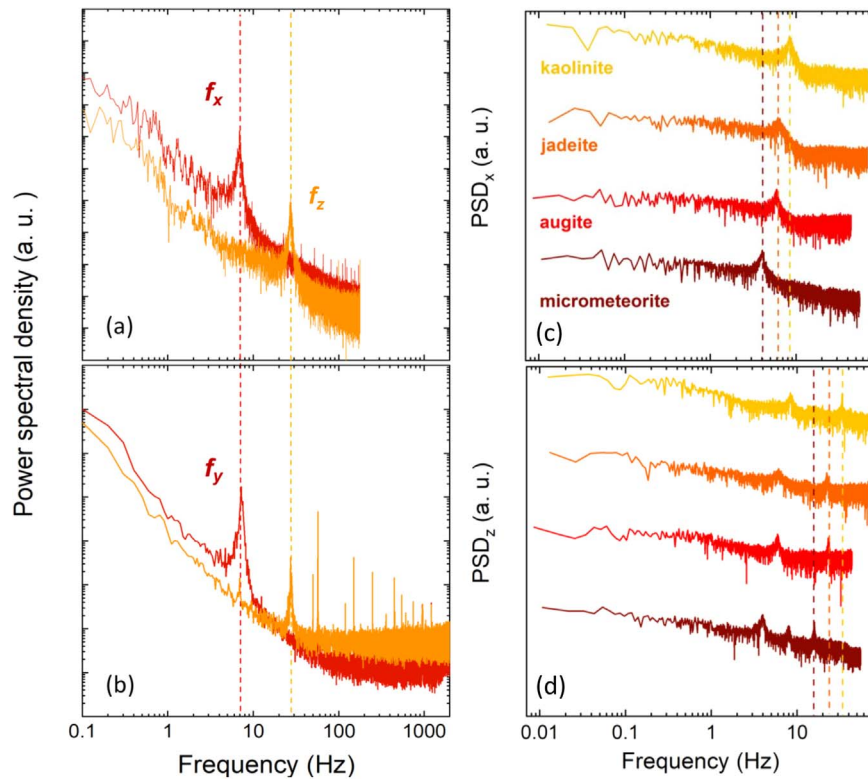


Figure 7. PSDs of a spherical bead and of cometary analogs. (a) Power spectra of a $R = 1.6$ mm spherical styrofoam particle obtained by using the tracking signals acquired by the CCD camera along the x transversal direction (f_x , red) and along the axial direction (f_z , orange). (b) Power spectra of signals obtained by the QPD detector along the y transversal direction (f_y , red) and along the axial direction (f_z , orange). Note that, due to the cylindrical symmetry of the trap, $f_x = f_y$. Power supply $V_{pp} = 4.5$ V. (c) PSD for the micrometeorite (brown), augite #1 (red), jadeite #2 (orange), and kaolinite (yellow) for particle fluctuations along the x direction. (d) PSD for the same particles in (c) but along the z direction. Power supply $V_{pp} = 15$ V. Dashed lines are used to highlight the increase in oscillation frequencies with decreasing material density (from the bottom to the top of each figure). Data have been displaced vertically for clarity.

one because it is originated by a photoluminescence emission of rare earth ions present in the mineral (B. L. Jolliff et al. 1996).

4. Conclusions

In conclusion, we have used acoustic levitation for the contactless manipulation of anhydrous and hydrated silicates in air (terrestrial analogs of cometary and asteroidal dust) and also chondritic material (fragments of the Saratov ordinary chondrite). The tracking of the particle in the trap and the PSD analysis of its dynamics allow the measurement of the particle volume and of the oscillation frequencies, which, in turn, can be used to calculate the trap spring constant if the particle density is known. Moreover, we demonstrate that the levitated particle can be successfully characterized with Raman spectroscopy and photoluminescence by coupling the levitator to a portable spectrometer. AL coupled with Raman spectroscopy has the potential to become a relevant technique for the contactless and noninvasive manipulation and characterization of millimeter-sized particles of extraterrestrial origin, while atmospheric contamination could be reduced by inserting the acoustic levitator and the Raman probe inside a sealed chamber with a controlled and inert atmosphere that could be helpful also to simulate planetary conditions. In addition, the PSD frequencies measured on the terrestrial analogs (see also Appendix B) could be used to infer the density of unknown samples of extraterrestrial origin, reducing their possible contaminations. In fact, a metrology of an unknown particle density could be obtained by levitating spherical samples of

known calibrated density. The measured trap frequencies on density-calibrated particles can be compared to the exact ones obtained from calculations of acoustic forces and trap spring constants based on the Gor'kov potential in order to obtain a correspondence between trap frequencies and density. Thus, such calibration could be used to interpolate the density of unknown samples. Knowing that sample-return missions (e.g., Hayabusa2 and OSIRIS-REx sampling C-complex asteroids Ryugu and Bennu, respectively) bring to Earth uncontaminated material in the form of millimetric and submillimetric dust (T. Yada et al. 2022), the use of AL has a great potential for their first characterization in receiving and curation facilities. Finally, due to the reduced size of the whole setup, AL could be part of payloads in future space missions for *in situ* analyses of dust particles on other planets.

Acknowledgments

This work has been funded by European Union (NextGeneration EU), through the MUR-PNRR project SAMOTHRACE (ECS00000022), PNRR MUR project PE0000023-NQSTI, the PRIN2022 "Cosmic Dust II" (grant No. 2022S5A2N7), "EnantioSelex" (2022P9F79R), "Flash-2D" (2022FWB2HE), "SEMPER" (20227ZXT4Z), the agreement ASI-INAF n.2018-16-HH.0, project "SPACE Tweezers," and the MSCA ITN project "ActiveMatter" (Horizon 2020, Project Number 812780), and carried out within the Project "Space It Up" funded by ASI and MUR – Contract n. 2024-5-E.0 - CUP n. I53D24000060005. Roberto Caruso is gratefully acknowledged for the technical help in the construction of the TinyLev.

Appendix A Appendix Information

A.1. Calibration of the Levitator with Styrofoam Spherical Particles




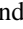


Spherical styrofoam particles ($\rho = 36 \text{ kg m}^{-3}$) have been used to test the setup. As styrofoam is very light, lower voltages than for analogs have been used as the power supply. Data have been recorded in the range of 4.5–8 V. Both detectors (the QPD and the CCD camera) have been used to acquire the particle position fluctuations in the trap. As expected due to the cylindrical symmetry of the trap, the transversal frequencies f_x and f_y measured on CCD and QPD (Figure 7 panels (a) and (b), respectively) agree with each other. Both detectors can record axial fluctuations, and the corresponding frequency (f_z in Figure 7) is the same. It is interesting to note that in these spectra no peak at $2 \times f_x$ is observed because the particle has a spherical shape. Other δ -like peaks above 50 Hz in PSDs obtained with the QPD detector are spurious signals, likely due to electronic noise, as they are observed also when no particles are in the trap or even when there is no light on the detector.

Appendix B

B.1. Other Cometary Analogs

Other cometary analogs (jadeite and kaolinite) have been trapped. The PSDs have been calculated from the video tracking of the particle center of mass. A comparison with PSDs obtained at $V_{pp} = 15 \text{ V}$ on the augite # 1 and the micrometeorite samples is shown in Figures 7(e) and (f). It is interesting to note that as $f_i \propto \sqrt{k_i/m}$, and both k_i and m are proportional to the volume V of the particle, f scales as $\sqrt{1/\rho}$, and thus, it is higher for less dense materials, at least when the Gorkov approximation is valid. In our case, jadeite ($\rho_{\text{jad}} = 3.3 \text{ gr cm}^{-3}$) and augite have a similar density, and the corresponding f_i are similar; on the contrary, kaolinite has a lower density ($\rho_{\text{kao}} = 2.6 \text{ gr cm}^{-3}$), and correspondingly, both its f_x and f_z are larger. On the basis of this analogy, it is possible to suggest that our micrometeorite has a higher density than augite because its oscillation frequencies are lower. The application of AL to the measurement of the bulk density of an unknown material of which only very small amounts are available (as in the micrometeorite case) is currently under investigation.

ORCID iDs

A. Foti  <https://orcid.org/0000-0002-9824-3099>
 A. Musolino  <https://orcid.org/0000-0003-1238-0445>
 L. Folco  <https://orcid.org/0000-0002-7276-3483>
 A. Mandanici  <https://orcid.org/0000-0002-3238-4948>
 O. M. Maragò  <https://orcid.org/0000-0002-7220-8527>
 M. G. Donato  <https://orcid.org/0000-0002-7580-3137>

References

- Anderson, O. L., & Liebermann, R. C. 1966, Vesiac State-of-the-Art Report 7885-4-X, 182, Willow Run Laboratories, The Institute of Science and Technology, The University of Michigan, <https://deepblue.lib.umich.edu/handle/2027.42/3282>
- Ashkin, A. 2006, Optical Trapping and Manipulation of Neutral Particles Using Lasers (Singapore: World Scientific)
- Baresch, D., & Garbin, V. 2020, *PNAS*, **117**, 15490
- Baresch, D., Thomas, J.-L., & Marchiano, R. 2016, *PhRvL*, **116**, 024301
- Barthelmy, D. 1997, Mineralogy Database; <http://webmineral.org>
- Blum, J., Gundlach, B., Krause, M., et al. 2017, *MNRAS*, **469**, S755
- Brearley, A. J., & Jones, R. H. 1998, Chondritic meteorites, Planetary Materials (Berlin: de Gruyter & Co)
- Brownlee, D. E., Tsou, P., Anderson, J. D., et al. 2003, *JGRE*, **108**, 8111
- Brunetto, R., Borg, J., Dartois, E., et al. 2011, *Icar*, **212**, 896
- Bruus, H. 2012, *Lab on a Chip*, **12**, 1014
- Cecchi-Pestellini, C., Iatì, M., & Williams, D. 2012, *JQSRT*, **113**, 2310
- Chan, Q. H. S., Stroud, R., Martins, Z., & Yabuta, H. 2020, *SSRv*, **216**, 56
- Chen, X., Ding, Q., Bi, C., Ruan, J., & Yang, S. 2022, *NatCo*, **13**, 7807
- Colangeli, L., Mennella, V., di Marino, C., Rotundi, A., & Bussoletti, E. 1995, *A&A*, **293**, 927
- Della Corte, V., Rietmeijer, F. J., Rotundi, A., Ferrari, M., & Palumbo, P. 2013, *TellB*, **65**, 20174
- Dangi, B. B., & Dickerson, D. J. 2021, *ACSOm*, **6**, 10447
- Della Corte, V., Rietmeijer, F. J. M., Rotundi, A., & Ferrari, M. 2014, *AsBio*, **14**, 694
- Della Corte, V., Palumbo, P., Rotundi, A., et al. 2012, *SSRv*, **169**, 159
- Dholakia, K., Drinkwater, B. W., & Ritsch-Marte, M. 2020a, *NatRP*, **2**, 480
- Dholakia, K., Drinkwater, B. W., & Ritsch-Marte, M. 2020b, *NatRP*, **2**, 513
- Ding, X., Lin, S.-C. S., Kiraly, B., et al. 2012, *PNAS*, **109**, 11105
- Ding, Z., Gao, H., Wang, C., et al. 2024, *AngCh*, **136**, e202317463
- Eigenbrode, J. L., Gold, R., Canham, J. S., et al. 2021, *FrST*, **2**, 734423
- El Hajjaji, A., & Ouladsine, M. 2001, *ITIE*, **48**, 831
- Ferrari, A. C., & Robertson, J. 2001, *PhRvB*, **64**, 075414
- Ferrari, M., Della Corte, V., Rotundi, A., & Rietmeijer, F. J. M. 2014, *P&SS*, **101**, 53
- Flynn, G. J., Keller, L. P., Feser, M., Wirick, S., & Jacobsen, C. 2003, *GeCoA*, **67**, 4791
- Folco, L., & Cordier, C. 2015, Planetary Mineralogy, ed. M. R. Lee & H. Leroux (European Mineralogical Union: Paris)
- Foresti, D., & Poulidakos, D. 2014, *PhRvL*, **112**, 024301
- Fulle, M., Della Corte, V., Rotundi, A., et al. 2016, *MNRAS*, **462**, S132
- Geim, A. K., Simon, M. D., Boamfa, M. I., & Heflinger, L. O. 1999, *Natur*, **400**, 323
- Genge, M. J., Engrand, C., Gounelle, M., & Taylor, S. 2008, *M&PS*, **43**, 497
- Gong, Z., Pan, Y.-L., Videen, G., & Wang, C. 2018a, *JQSRT*, **214**, 94
- Gong, Z., Pan, Y.-L., Videen, G., & Wang, C. 2018b, *AcAc*, **1020**, 86
- Grady, M. M. 2000, Catalogue of Meteorites (Cambridge: Cambridge Univ. Press)
- Helander, P., Puranen, T., Merilainen, A., et al. 2020, *ApPhL*, **116**, 19
- Jolliff, B. L., Freeman, J. J., & Wopenka, B. 1996, *LPSC*, **27**, 613
- Jones, P. H., Palmisano, F., Bonaccorso, F., et al. 2009, *ACSNa*, **3**, 3077
- Jones, P. H., Marago, O. M., & Volpe, G. 2015, Optical Tweezers (Cambridge: Cambridge Univ. Press)
- Joswiak, D., Brownlee, D., Nguyen, A., & Messenger, S. 2017, *M&PS*, **52**, 1612
- Kohout, T., Kallonen, A., Suuronen, J.-P., et al. 2014, *M&PS*, **49**, 1157
- Koyama, D., & Nakamura, K. 2010, *ITUFF*, **57**, 1152
- Lafuente, B., Downs, R. T., Yang, H., et al. 2015, Highlights in Mineralogical Crystallography, (Berlin: de Gruyter)
- Lin, S. 1995, *Ultra*, **33**, 445
- Liu, Y., Pan, J., Zhang, G., et al. 2023, *AAMI*, **15**, 33037
- Luo, T., Liu, S., Zhou, R., et al. 2023, *Lab on a Chip*, **23**, 3989
- Ma, Z., Holle, A. W., Melde, K., et al. 2020, *AdM*, **32**, 1904181
- Marrara, S., Ciriza, D. B., Magazzu, A., et al. 2023, *ITIM*, **72**, 9600808
- Marzo, A., Barnes, A., & Drinkwater, B. W. 2017, *RSci*, **88**, 085105
- Marzo, A., & Drinkwater, B. W. 2019, *PNAS*, **116**, 84
- Marzo, A., Seah, S. A., Drinkwater, B. W., et al. 2015, *NatCo*, **6**, 8661
- McGuire, B. A. 2018, *ApJS*, **239**, 17
- Memoli, G., Caleap, M., Asakawa, M., et al. 2017, *NatCo*, **8**, 14608
- Meng, L., Cai, F., Li, F., et al. 2019, *JPhD*, **52**, 273001
- Messenger, S., Brownlee, D., Joswiak, D., & Nguyen, A. 2015, *LPSC*, **32793**, 2603
- Morris, R. H., Dye, E. R., Docker, P., & Newton, M. I. 2019, *PhFI*, **31**, 101301
- Ospina, J. F. P., Contreras, V., Estrada-Morales, J., et al. 2022, *PhRvP*, **18**, 034026
- Ozcelik, A., Rufo, J., Guo, F., et al. 2018, *NatMe*, **15**, 1021
- Park, J., Min, A., Theerthagiri, J., Ashokkumar, M., & Choi, M. Y. 2023, *UItS*, **94**, 106345
- Perltz, J. F. A., Gentner, L., Braeuer, P. A. B., & Will, S. 2022, *Sensors*, **22**, 1111
- Puskar, L., Tuckermann, R., Frosch, T., et al. 2007, *Lab on a Chip*, **7**, 1125
- Ralph, J. 2000, Mindat.org, <http://www.mindat.org>
- Rietmeijer, F. J. M., Della Corte, V., Ferrari, M., Rotundi, A., & Brunetto, R. 2016, *Icar*, **266**, 217

- Rietmeijer, F. J. 1998, *Planetary Materials* (Berlin: de Gruyter)
- Rietmeijer, F. J. M. 2002, *ChEG*, **62**, 1
- Rochette, P., Folco, L., Suavet, C., et al. 2008, *PNAS*, **105**, 18206
- Rotundi, A., Brucato, J., Colangeli, L., et al. 2002, *M&PS*, **37**, 1623
- Rotundi, A., Ferrini, G., Baratta, G., et al. 2007, Combined Micro-Infrared (IR) and Micro-Raman Measurements on Stratospheric Interplanetary Dust Particles, Workshop on Dust in Planetary Systems, 643, ed. H. Krueger & A. Graps (Kauai, Hawaii), 149
- Rotundi, A., Rietmeijer, F., Ferrari, M., et al. 2014, *M&PS*, **49**, 550
- Rubinsztein-Dunlop, H., Nieminen, T., Friese, M., & Heckenberg, N. 1998, *AdQC*, **30**, 469,
- Sandford, S. A. 2011, *IAUS*, **280**, 275
- Smith, C. L., Russell, S. S., Hutzler, A., et al. 2021, Sample Return Missions, ed. A. Longobardo (Amsterdam: Elsevier), 249
- Taylor, S., Messenger, S., & Folco, L. 2016, *Elements*, **12**, 171
- Thalhammer, G., McDougall, C., MacDonald, M. P., & Ritsch-Marte, M. 2016, *Lab on a Chip*, **16**, 1523
- Tsuda, Y., Yoshikawa, M., Abe, M., Minamino, H., & Nakazawa, S. 2013, *AcAau*, **91**, 356
- van Ginneken, M., Wozniakiewicz, P. J., Brownlee, D. E., et al. 2024, *RSPTA*, **382**, 20230195
- Whymark, R. R. 1975, *Ultra*, **13**, 251
- Yada, T., Abe, M., Okada, T., et al. 2022, *NatAs*, **6**, 214
- Yada, T., Abe, M., Nishimura, M., et al. 2023, *EP&S*, **75**, 170
- Yamaguchi, T., Hata, N., Matsuo, S.-I., et al. 2023, *Analytical Sciences*, **39**, 977
- Yoshikawa, M., Kawaguchi, J., Fujiwara, A., & Tsuchiyama, A. 2021, Sample Return Missions, ed. A. Longobardo (Amsterdam: Elsevier), 123
- Zang, D., Yu, Y., Chen, Z., et al. 2017, *AdCIS*, **243**, 77